Iraqi Journal of Physics, 2025 *Vol.23, No.3, PP.104-113*
https://doi.org/10.30723/ijp.v23i3.1277 *P-ISSN: 2070-4003*
E-ISSN: 2664-5548

Synthesis and Optical Characterization of (Cu:Se) Nanoparticles Prepared via Atmospheric Pressure Plasma Jet for UV Detector and Gas Sensor Applications

Doaa Rifaat Jassim[1], Ramiz Ahmed Al-Ansari[2*], and Ban H. Adil[2]
[1]*Forensic Science, College of Sciences, AL-Nahrain University, Baghdad, Iraq*
[2]*Department of Physics, College of Science for Women, University of Baghdad, Baghdad, Iraq*
[*]Corresponding author: ramizam_phys@csw.uobaghdad.edu.iq

Abstract
The created copper selenide (Cu:Se) nanoparticles were used in experiments for detecting UV light and in gas sensors. This research prepared Cu:Se nanoparticles with different ratios of 1:9, 2:8, and 3:7 using an atmospheric pressure plasma jet technique. The study looked at the optical properties of Cu:Se nanoparticles using X-ray diffraction (XRD) analyses, which showed that adding more Se made the crystals larger. UV–visible spectroscopy and the calculation of band gap energy were performed. All ratios yielded high transmission values, ranging from 80% to 95%. The band gap energy was found to be 3.80 eV, 3.25 eV, and 4.17 eV for the Cu:Se ratios of 1:9, 2:8, and 3:7, respectively, which are typical and excellent values for semiconductors. The prepared Cu:Se nanoparticles demonstrated good optical properties. The optical absorbance of Cu:Se NPs is in order in the wide region of λ = 200 to 350 nm, which is suitable for UV absorbance materials.

Article Info.

Keywords:
Cu:Se Nanoparticles, Plasma Jet, UV–Vis Spectroscopy, Optical Properties, Band Gap Energy.

Article history:
Received: Apr. 15, 2024
Revised: Oct. 31, 2024
Accepted:Nov.22, 2024
Published:Sep. 01,2025

1. Introduction

In recent years, many studies have been conducted on metallic nanoparticles (NPs) due to their favorable electronic, mechanical, and optical properties [1]. The focus on copper and copper selenide (Cu:Se) NPs has opened up broad perspectives in research and application with nanometer-scale components. These nanoparticles have good mechanical stability and incorporate different components that determine optical features, providing both convenient research and various application interests. While there has been less research on copper compound nanoparticles with large surface area, tiny grain size, strong chemical activity, and high thermal stability [2, 3]. The composite NPs usually have a diameter between 20 and 200 nm and are synthesized in different forms, such as wires, tubes, rings, cubes, spheres, and so on. Several preparation techniques for nanomaterials are available, including hydrothermal techniques, sol-gel preparation, chemical precipitation, thermal decomposition, and pulsed laser deposition [4, 5]. Microwave and plasma jet technology have recently drawn much attention as the top "green technologies" for synthesizing nanomaterials since they are inexpensive, environmentally friendly, and don't require expensive equipment [6-8]. To create nanomaterials, plasma-generated reactive oxygen and nitrogen species (RONS) must interact with liquids because they alter the liquid's chemical makeup. The main RONS that are produced during plasma-liquid interactions are singlet oxygen. The effectiveness of argon in plasma jet technology makes it a good method for preparing Cu:Se nanoparticles because it is inexpensive and safe to use [9, 10]. This study involves the effect of the Cu concentration to grow uniformly sized and distributed Cu:Se NPs. Increasing colloidal stability through metal selenide capping may also be a useful technique for gas sensors, electrical rectifiers, X-ray machines, or tumor treatment [11, 12]. This study aims to synthesize Cu:Se nanoparticles using an atmospheric pressure

plasma jet technique, evaluate their optical properties, and investigate the Cu:Se concentration influence on particle uniformity and colloidal stability, with potential applications in UV detectors, gas sensors, and other advanced technologies.

2. Preparation of Nanoparticle

2. 1. Preparation of the Chemical Solution

The chemical solution of copper and selenium were prepared as follows:

A - Preparation of copper solution: The copper solution used copper (II) carbonate. 0.5 mM of copper (II) carbonate salts ($CuCO_3$) was added to a designated cup of distilled water and the required concentration (mol^{-1}) was calculated according to Eq.(1)

$$\text{Concentration(mole/liter)} = \text{mass(g)/molecular(g/mol)} \times \text{volume(liter)} \quad \textbf{(1)}$$

B - Preparation of Selenium Solution: Selenium nitrate $SeO(NO_3)_2$ is used to prepare the solution. In this step, 0.5mM concentration of Selenium nitrate will be added to a distilled water dedicated beaker and Eq.(1) is used to calculate the required concentration (mole $^{-1}$), and then we move to the next step.

2. 2. Preparation of Cu NPs

The copper and selenium nanoparticles using the plasma jet method under atmospheric pressure were prepared according to the following steps:

The prepared copper salts solution of the required concentration and size was placed on the holder under the metal tube, as mentioned above. The cup was brought closer to the metal tube, and the distance between the liquid surface and the tube nozzle was 1 cm.

A flow meter set at 3 (l/min) was used to regulate the flow of the argon gas (of 99.99% purity) as the discharge gas flowing into a stainless-steel tube, of 1 mm inner diameter, connected to the cathode. The argon gas allowed the plasma jet to spread, and roughly 1 cm separated the plasma jet nozzle from the distilled water surface.

The solution for the copper nanoparticles was placed in a beaker, which holds 20 mL of liquid. The voltage value supplied to the system was gradually increased until plasma was generated between the tube and the liquid surface. The solution was subjected to the plasma for 30 minutes, after which the color of the solution changed to a dark olive color due to the reaction process indicating the synthesis of copper nanoparticles, as shown in Fig. 1.

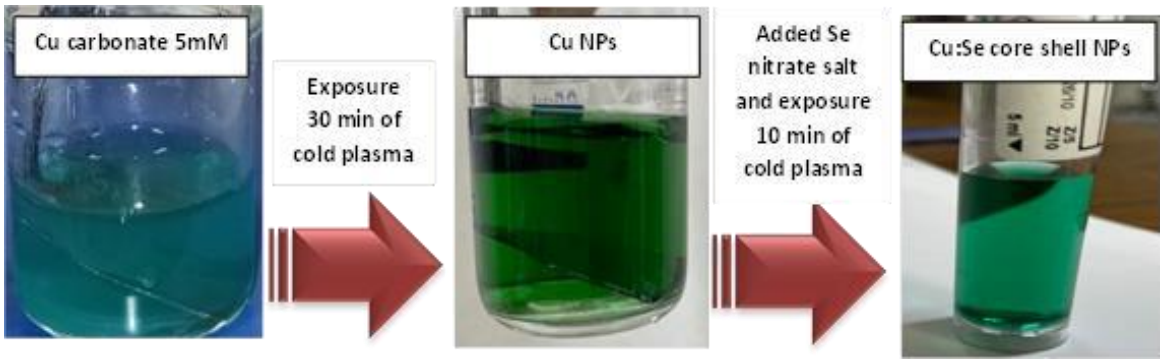

Figure1: Synthesis of Cu:Se NPs by plasma jet [9].

2. 3. Synthesize Procedure of Cu:Se Nanoparticles

To prepare Cu:Se core-shell of 3:7 NPs, 3 mL of Cu NPs was mixed well with 7 mL of Se nitrate salt in a flask, and then placed under the cold plasma system for 10 min to produce Cu:Se NPs. In the same way, the other samples of Cu:Se NPs with 2:8 and 1:9 ratios were prepared.

A UV-Vis-NIR Metrotech dual-beam spectrometer was used to measure the produced Cu:Se NPs and capture the absorption spectra of the thin films, which were made using the spin coating approach, in the 200–1100 nm wavelength range.

3. Results and Discussion

Fig. 2 depicts the X-ray diffraction (XRD) patterns of Cu:Se NPs deposited on quartz substrates with different Cu:Se atomic ratios of 3:7, 2:8, and 1:9. The sample with minimal Se content exhibited a low crystallinity configuration, while an increase in Se content led to a significant improvement in sample crystallinity, resulting in a well-defined Cu:Se polycrystalline structure. This crystalline phase was identified as the hexagonal klockmannite phase (Pmmc 63) of Cu:Se corresponding to standard card (JCPDS No. 34-0171), with visible diffraction peaks at 2θ= 28.2093°, 31.2260°, 46.0375°, 50.1875°, 56.6243°, 28.1670°, 31.2160°, 45.9952°, 50.0605°, and 56.7514°, corresponding to the crystalline planes with Miller indices of (102), (006), (110), (108), (116), (102), (006), (110), (108), and (116), respectively. This structural configuration aligns with the results of Liu et al. [13]. Notably, all three samples exhibited a preferred orientation along the (006) crystallographic direction. An additional small peak located at 29.6 ° corresponds to the (101) direction of the Se structure [14]. The systematic crystallinity control through the Cu: Se ratio offers a promising approach to tailor their properties for specific applications, influencing optical and electrical properties. This renders them suitable candidates for various devices. Furthermore, the customized orientation of thin films along specific crystallographic directions can be exploited in advancing sensor technologies [15].

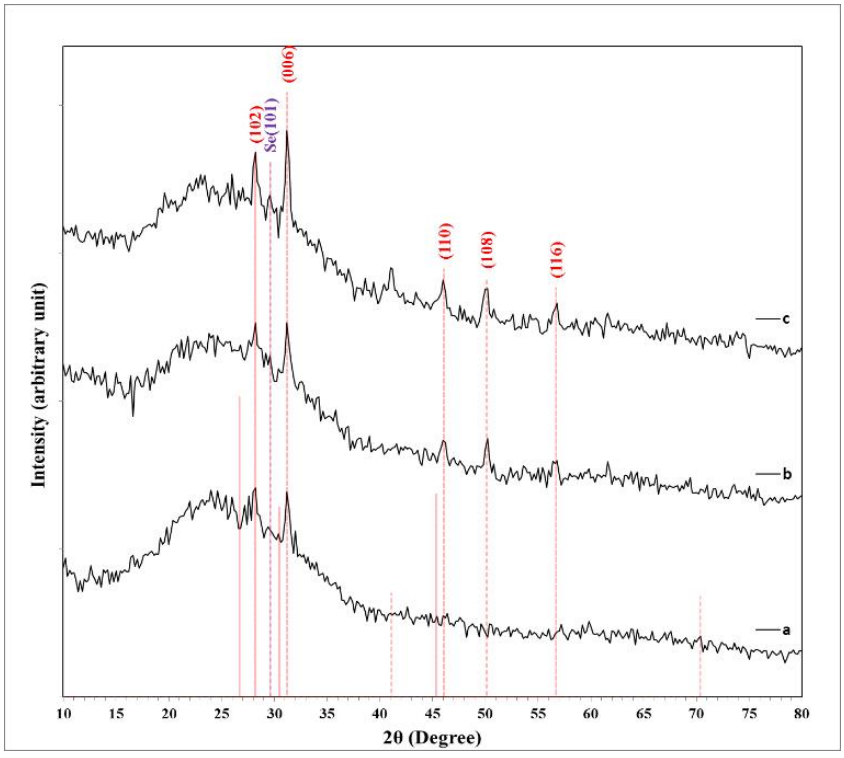

Figure 2: XRD patterns of CuSe core-shell deposited at different Cu: Se atomic ratios of (a) 3:7, (b) 2:8, and (c)1:9.

The Bragg equation (Eq. (2)) was utilized to determine the inter-planar spacing (d_{hkl}), while Scherrer's formula was applied to calculate crystal size (D), as summarized in Table 1.

By the lattice constant relation for the Hexagonal structure [16]

$$\frac{1}{d_{hkl}{}^2} = \frac{4}{3}\frac{h^2 + hk + k^2}{a^2} + \frac{l^2}{c^3} \quad (2)$$

where d_{hkl} represents the interplanar spacing, and a and c denote the lattice constants. The lattice constants (a and c) were determined utilizing the d_{hkl} values corresponding to the (102) and (006) directions.

Table 1: XRD parameters of Cu:Se NPs deposited at different Cu:Se atomic ratios.

Sample	2θ (Deg.)	FWHM (Deg.)	d_{hkl} Exp.(Å)	D (nm)	hkl	ε
3:7	28.2570	0.7199	3.1557	11.4	(102)	0.0030
	31.2583	0.6770	2.8592	12.2	(006)	0.0028
2:8	28.2093	0.6690	3.1609	12.2	(102)	0.0028
	31.2260	0.5929	2.8621	13.9	(006)	0.0025
	46.0375	0.6770	1.9699	12.7	(110)	0.0027
	50.1875	0.5505	1.8163	15.9	(108)	0.0022
	56.6243	0.7622	1.6242	11.8	(116)	0.0029
1:9	28.1670	0.5082	3.1656	16.1	(102)	0.0022
	29.6000	0.4200	3.0155	19.6	(101) Se	0.0018
	31.2160	0.4230	2.8630	19.5	(006)	0.0018
	45.9952	0.5082	1.9716	17.0	(110)	0.0020
	50.0605	0.5929	1.8206	14.8	(108)	0.0023
	56.7514	0.5505	1.6208	16.4	(116)	0.0021

As demonstrated in Table 2, the lattice parameters (a and c) closely approximated their reported values in JCPDS No. 34-0171. Additionally, both lattice constants increased with the rise in Se content. This observation suggests that the strain in the lattice, induced by nanoscale particles at low Se content, diminishes with an increase in the crystallite size. The observed increase in lattice constant with increasing Se content indicates a correlation between Se content and the crystalline structure. As more Se content is introduced, the individual crystallites may grow in size, resulting in a reduction in lattice strain. However, as the crystallite size increases, internal strain diminishes. This can be attributed to a more relaxed lattice structure as the particles grow and the stress is distributed over a larger area [17].

Table 2: Lattice constants of (Cu:Se) NPs deposited at different Cu: Se atomic ratios.

Cu:Se	a (Å)	c (Å)
3:7	3.91873	17.1553
2:8	3.92562	17.1726
1:9	3.93211	17.1779

UV-Vis spectroscopy was used to investigate the optical absorption properties of Cu:Se NPs produced by the atmospheric plasma jets process and deposited on quartz substrate. The optical characterization of the NPs provided information about physical properties, such as absorbance and band gap energy. Plotting the experimental absorbance data is a common method to measurethe optical band gap of NPs.

Fig. 3 illustrates the UV–Vis absorbance spectra of Cu:Se NPs thin films prepared using various amounts of Cu NPs. Based on the spectra, it is evident that the samples 1:9, 2:8, and 3:7 exhibit the plasmon band at 247, 259, and 262 nm, respectively, indicating that Cu NPs were formed. Surface plasmon resonance of Cu and Se nanoparticles displayed broad bands and shifted to a higher wavelength of 530-550nm

(redshift) due to the increased Cu NPs. It is clear that the Cu:Se NPs have three regions: the first one between 210 and 214nm for CuO NPs, the second between 240 and 262nm for Se NPs, and the third between 360 and 370 nm for Cu NPs. These results exactly match previously reported results [18-20]. An absorbance spectrum showed an increase in the plasmon peak with increasing the concentration of Cu, indicating an increase in the concentration of NPs.

The transmittance spectra of Cu:Se NPs with different concentration ratios of Cu:Se (1:9, 2:8 and 3:7) showed that transmittance increased with increasing Cu concentration in the wavelength range of 400 to 1100 nm at room temperature. All tests gave a high transmission value of about 89% to 95%, as seen in Fig. 2, but different in the transition response, where the copper nanoparticles start to work at the process region of about 400 nm.

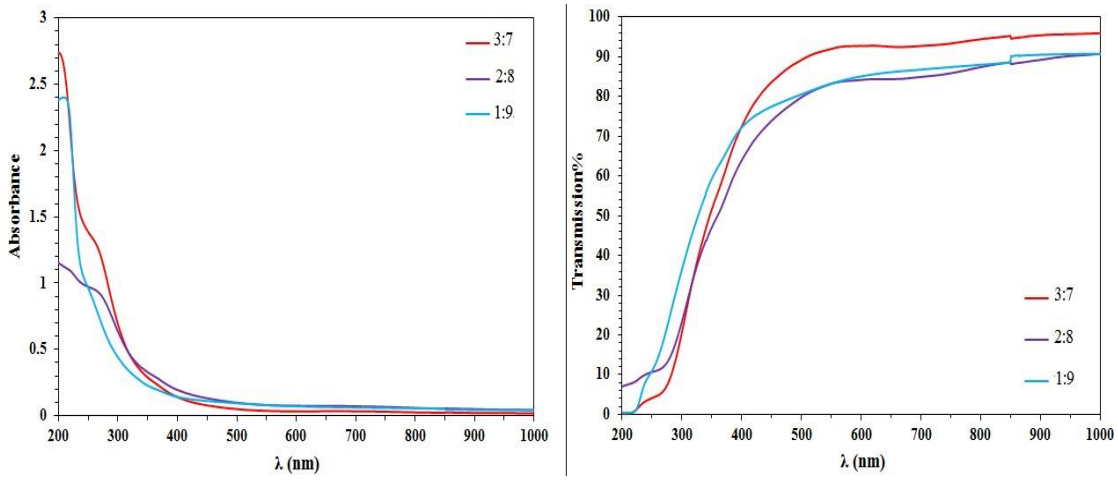

Figure 3: UV–VIS absorbance and transmittance spectra of Cu:Se NPs at different ratio.

Fig. 4 shows the absorption coefficient and band gap of Cu:Se of (1:9, 2:8 and 3:7) NPs. The spectra indicated strong absorption in the UV region and a redshift. This might result from the Cu and Se ions interactions. The absorbed light shifted toward the red end of the visible spectrum as the concentration ratio of copper was increased. This shift is beneficial for photocatalytic activity because it allows light to penetrate the inner surface and reflect several times. Eq.(3) illustrates the direct measurement of the band gap using Planck's law[21]:

$$E_g = \frac{hc}{\lambda_{cut}} = \frac{1240}{\lambda_{cut}} \quad \textbf{(3)}$$

where c= (3×10^8 m/s) is the light velocity, h= (6.626×10^{-34} Js) is Planck's constant, and λ_{cut} is the cut-off wavelength that corresponds to the optical bandgap. The absorption coefficients of the Cu:Se NPs coating were graphically estimated using the Tauc relationship (Eq. (4)) for a direct transition to better study the optical properties of the coating [22, 23] :

$$\alpha h\upsilon = A\,(h\upsilon - E_g)^r \quad \textbf{(4)}$$

where r is a value that depends on the nature of the transition type; r =2 for the permitted direct transition, A is a constant equal to 0.9, υ is the incident photon frequency, h is Planck's constant, and α is the absorption coefficient. Plotting a graph between the photon energy (hυ) and $(\alpha h\upsilon)^r$ is a common method for determining a band gap by extrapolating the straight line to intercept the (hυ) axis. Fig. 4 shows the Tauc plots

for the different concentrations of Cu:Se (1:9,2:8 and 3:7) NPs deposited on quartz substrates. The optical band gaps associated with NPs vary in value across all data. The band gap values for the (Cu: Se) NPs coating of different concentrations of Cu:Se (1:9,2:8 and 3:7) were 4.30, 3.80 and 4.17 eV, respectively [24]. The decrease in the optical energy gap may be due to structural defects and more oxygen and copper atoms diffusing into the band gap at specific levels [25-28]. For the various Cu:Se ratios, the variation in distance between the atoms caused lattice strain, which is a factor that influences the value of the optical energy gap. Because of the preparation conditions and the degree of crystallization of the prepared samples, the energy gap values differ from the expected values; the presence of tail states within the band gap may explain the band gap values [29]. The results agree with the work [30]. Which suggests that the produced films have good optical quality due to low scattering or absorption losses [31].

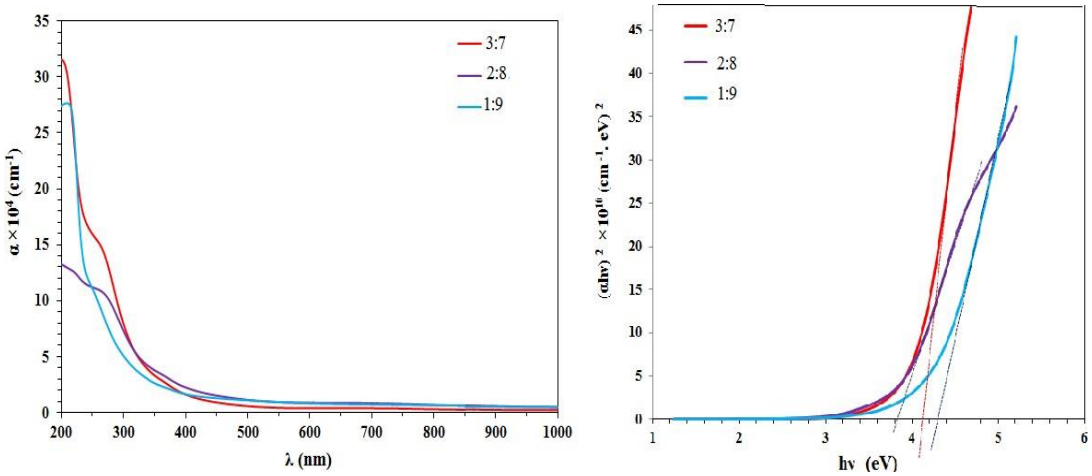

Figure 4: The absorption coefficient and band gap of (Cu: Se) NPs at different ratio.

The refractive index might be a significant parameter when considering optical materials and applications. Based on reflectance (R) data, the index of refraction for (Cu: Se) NPs that were deposited was determined [32-34].

$$n = \sqrt{\frac{4R}{(R-1)} - K^2 - \left[\frac{(R+1)}{(R-1)}\right]} \qquad (5)$$

Fig. 5 shows the refractive indices of Cu:Se NPs as a function of wavelength. It can be seen that the refractive index declines along with the wavelength rise (anomalous dispersion). The behavior here is owing to the increase in the energy gap. The differential in optical absorption between the visional and ultraviolet areas may be the reason for the variance in refractive indices in the ultraviolet visible regions with various copper concentration ratios. The relationship between the coefficients of extinction and absorption is [35]

$$K = \frac{\alpha\lambda}{4\pi} \qquad (6)$$

The extinction coefficient of a Cu:Se NPs could easily be determined from Fig. 4. Because this coefficient depends on the absorption coefficient, it may behave similarly to the absorption coefficient. It is evident that the extinction coefficient increases in the UV range with the copper concentration ratio.

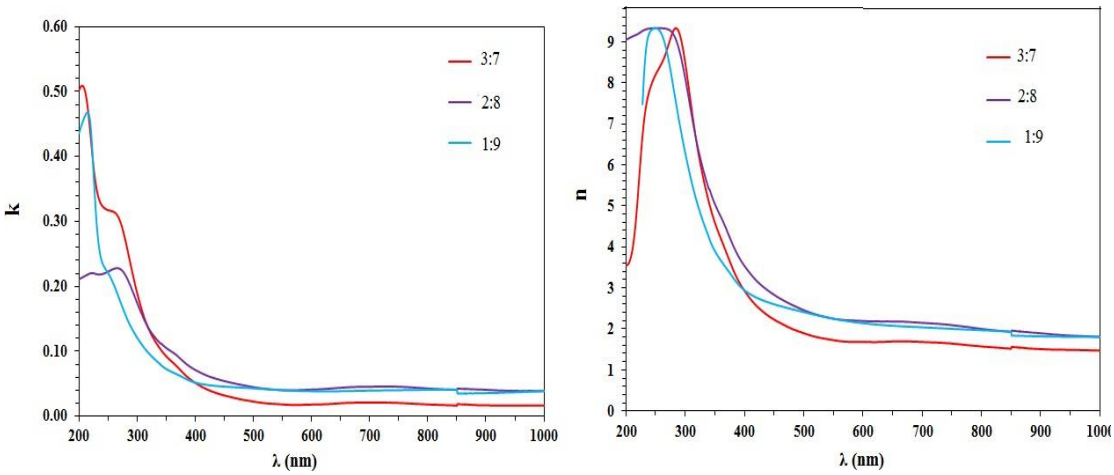

Figure 5: The refractive index and extinction coefficient of (Cu: Se) NPs at different ratio.

The dielectric constant is given by [35]

$$\varepsilon=\varepsilon_r-i\varepsilon_i \quad \textbf{(7)}$$

The real (ε_r) and imaginary (ε_i) dielectric constant parts can be related to the values of n (refractive index) and the values of k (extinction coefficient). Those values are counted utilizing the formulas below [35]

$$\varepsilon_r = n^2_o-k^2_o \quad \textbf{(8)}$$

$$\varepsilon_i =2n_ok_o \quad \textbf{(9)}$$

Fig. 6 presents the dependence of the dielectric constant (real (ε_r) and imaginary (ε_i) values) of a Cu:Se NPs coating on wavelength. The values of the real part are greater than those of the imaginary part, and both the real and imaginary parts follow the same pattern. It is evident that as wavelength increased, both the real and imaginary parts of the dielectric constant decreased. As the ratio of copper concentration grows, both constants rise along the visible region. The refractive index value determines the difference in the dielectric constant. Conversely, the extinction coefficient values in relation to the absorption difference determine the dielectric loss [36].

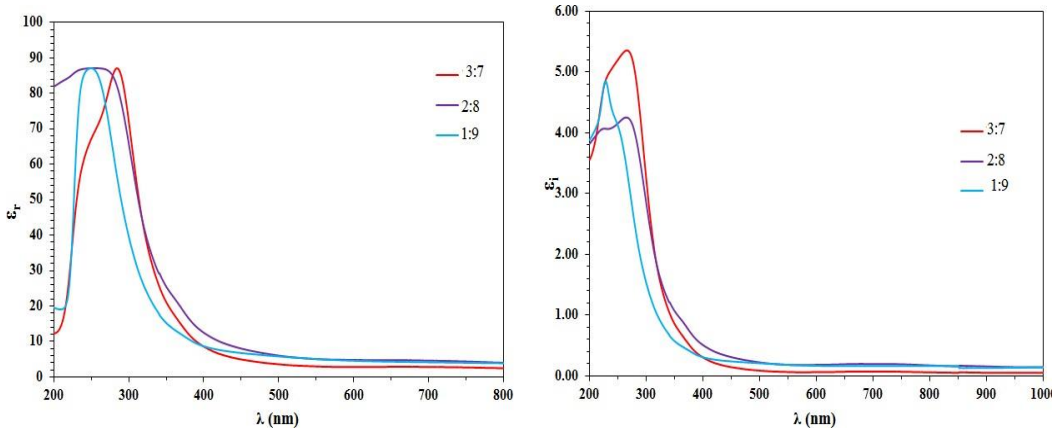

Figure 6: The real (ε_r) and imaginary (ε_i) dielectric constants of Cu:Se NPs at different ratio.

Cu:Se NPs' optical conductivity (ϭ) depends on the optical band gap as well as on several other factors, such as the frequency of incident photons, the refractive index, the

extinction coefficient, and the absorption coefficient. The relationship below can be used to calculate the optical conductivity [37-39]

$$\sigma = \frac{\alpha nc}{4\pi k} \quad \textbf{(10)}$$

Fig. 7 illustrates the optical conductivity (σ) increase in the ultraviolet region with theincrease in the ratio of copper concentration. Due to that, the electrons continue to excite the produced charge carriers as the falling photon's energy increases, resulting in the generation of optical current. Because all electrons in the visible wavelength region have low energy and are constrained by their holes in the valence band, the optical conductivity σ falls as the ratio of copper concentration increases. As a result, the pair (e-h) is not producing any current [39].

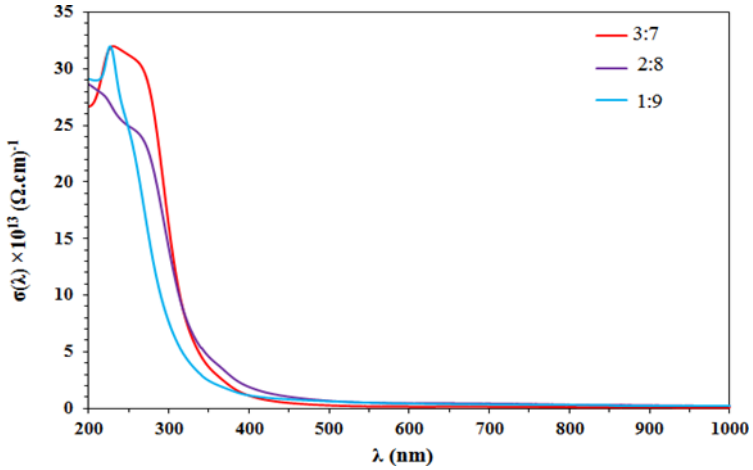

Figure 7: The optical conductivity σ of (Cu: Se) NPs at different ratios.

Table 3 shows variations in absorbance, absorbance coefficient, refractive index, extinction coefficient, real (ε_r) and imaginary (ε_i) dielectric constant parts and optical energy gap at λ = 500nm for (Cu: Se) NPs prepared using a different concentration of Cu NPs.

Table3: The optical properties parameters at λ = 500nm for (Cu: Se) NPs at different ratio.

Cu:Se NPs	α (cm^{-1})	K	n	E_r	E_i	E_g (eV)
3:7	5739	0.023	1.898	3.601	0.087	4.17
2:8	11306	0.045	2.458	6.042	0.221	3.80
1:9	10825	0.043	2.411	5.813	0.208	4.30

4. Conclusions

The atmospheric plasma jet technique successfully synthesized Cu:Se NPs at different concentrations of Cu. So, the plasma jet technique appears to be a strong method for creating nanoparticles with special optical features for various uses, like photodiodes.

Acknowledgements

The authors would like to thanks the University of Baghdad, Collage of Science, Department of Physics, for assist us in this article.

Conflict of Interest

Authors declare that they have no conflict of interest.

References

1. M. K. Khalaf, R. M. S. Al-Alwany, and I. K. Salman, J. Crit. Rev. **7**, 171 (2020). https://doi.org/10.1142/S0219581X23500758.
2. H. S. A. Al-Shmgani, W. H. Mohammed, G. M. Sulaiman, and A. H. Saadoon, Artif. Cell. Nanomed. Biotech. **45** (6), 1234 (2016).https://doi.org/10.1080/21691401.2016.1220950.
3. M. K. Ahmed, R. Al-Wafi, S. F. Mansour, S. I. El-Dek, and V. Uskoković, J. Mat. Res. Tech. **9**, 3710 (2020). https://doi.org/10.1016/j.jmrt.2020.01.108 .
4. R. Sagheer, S. T. Khadija, Z. N. Kayani, and S. Riaz, Optik **244**, 166816 (2021). https://doi.org/10.1016/j.ijleo.2021.166816.
5. T. Tenzin, B. Neena, R. J, P. N. Kumar, and J. M. Shyla, Mat. Sci. Poland **33**, 826 (2015). https://doi.org/10.1515/msp-2015-0097.
6. L. N. Nguyen, P. Lamichhane, E. H. Choi, and G. J. Lee, Nanomaterials **11**(7), 1678 (2021). https://doi.org/10.3390/nano11071678.
7. J. Wojnarowicz, T. Chudoba, and W. Lojkowski, Nanomaterials **10**(6), 1086 (2020). https://doi.org/10.3390/nano10061086.
8. M. Sajjad, I. Ullah, M. I. Khan, J. Khan, M. Y. Khan, and M. T. Qureshi, Res. Phys. **9**, 1301 (2018). https://doi.org/10.1016/j.rinp.2018.04.010.
9. D. R. Jassim, R. A. Al-Wasiti, and B. H. Adil, Plasma Med. **13**, 31 (2023). https://doi.org/10.1615/PlasmaMed.2023049445.
10. A. N. Mohsin, R. A. Al-Ansari, and B. H. Adil, *AIP Conf. Proc*. **2437**, 020095 (2022). https://doi.org/10.1063/5.0092551.
11. X. Cao, Y. Xie, and L. Li, Adv. Mat. **15**, 1914 (2003). https://doi.org/10.1002/adma.200305519.
12. J.-L. Li and X.-Y. Liu, J. Nanosci. Nanotech. **8**, 2488 (2008). https://doi.org/10.1166/jnn.2008.502.
13. Y.-Q. Liu, F.-X. Wang, Y. Xiao, H.-D. Peng, H.-J. Zhong, Z.-H. Liu, and G.-B. Pan, Sci. Rep. **4**, 5998 (2014). https://doi.org/10.1038/srep05998.
14. F. Jiang, W. Cai, and G. Tan, Nanoscal. Res. Lett. **12**, 401 (2017). https://doi.org/10.1186/s11671-017-2165-y.
15. M. R. Scimeca, F. Yang, E. Zaia, N. Chen, P. Zhao, M. P. Gordon, J. D. Forster, Y.-S. Liu, J. Guo, J. J. Urban, and A. Sahu, ACS Appl. Ener. Mat. **2**(2), 1517 (2019). https://pubs.acs.org/doi/abs/10.1021/acsaem.8b02118.
16. I. G. Shitu, K. K. Katibi, L. S. Taura, A. Muhammad, I. M. Chiromawa, S. B. Adamu, and S. G. Durumin Iya, Ceram. Int. **49**, 12309 (2023). https://doi.org/10.1016/j.ceramint.2022.12.086.
17. T. P. Vinod, X. Jin, and J. Kim, Mat. Res. Bullet. **46**, 340 (2011). https://doi.org/10.1016/j.materresbull.2010.12.017.
18. G. K. Prashanth, P. A. Prashanth, P. Singh, B. M. Nagabhushana, C. Shivakumara, G. M. Krishnaiah, H. G. Nagendra, H. M. Sathyananda, and V. Chaturvedi, J. Asian Ceram. Soci. **8**, 1175 (2020). https://doi.org/10.1080/21870764.2020.1824328.
19. V. Perumal, U. Hashim, S. C. B. Gopinath, H. Rajintra Prasad, L. Wei-Wen, S. R. Balakrishnan, T. Vijayakumar, and R. A. Rahim, Nanoscal. Res. Lett. **11**, 31 (2016). https://doi.org/10.1186/s11671-016-1245-8.
20. M. A. Fakhri, Eng. Tech. J. **32**, 1323 (2014).
21. A. A. Ali, Y. S. Rammah, R. El-Mallawany, and D. Souri, Measurement **105**, 72 (2017). https://doi.org/10.1016/j.measurement.2017.04.010.
22. A. I. Khudiar, M. K. Khalaf, and A. M. Ofui, Opt. Mat. **114**, 110885 (2021). https://doi.org/10.1016/j.optmat.2021.110885.
23. V. I. Klimov, Annual Rev. Phys. Chem. **58**, 635 (2007). https://doi.org/10.1146/annurev.physchem.58.032806.104537.
24. E. P. Domashevskaya, V. V. Gorbachev, V. A. Terekhov, V. M. Kashkarov, E. V. Panfilova, and A. V. Shchukarev, J. Elect. Spect. Relat. Phenom. **114-116**, 901 (2001). https://doi.org/10.1016/S0368-2048(00)00406-0.
25. K. V. Yumashev, V. S. Gurin, P. V. Prokoshin, V. B. Prokopenko, and A. A. Alexeenko, Phys. Stat. Sol. B **224**, 815 (2001). https://doi.org/10.1002/(SICI)1521-3951(200104)224:3<815::AID-PSSB815>3.0.CO;2-H.
26. K. V. Yumashev, N. N. Posnov, I. A. Denisov, P. V. Prokoshin, V. P. Mikhailov, V. S. Gurin, V. B. Prokopenko, and A. A. Alexeenko, J. Opt. Soci. America B **17**, 572 (2000). https://doi.org/10.1364/JOSAB.17.000572.
27. M. K. Khalaf, F. S. Ahmed, and R. M. S. Al-Alwany, Egyp. J. Chem. **63**, 281 (2020). https://doi.org/10.21608/ejchem.2019.17350.2064.
28. H. D. Abdullah, H. F. Al-Taay, M. K. Khalaf, H. F. Oleiwi, and A. J. Rahma, J. Phys. Conf. Ser. **2114**, 012074 (2021). https://doi.org/10.1088/1742-6596/2114/1/012074.
29. J. Damisa and J. O. Emegha, Tren. Sci. **18**, 16 (2021). https://doi.org/10.48048/tis.2021.16.

30. S. Q. Haza'a and H. R. Shaker, Int. J. Thin Fil. Sci. Tech. **7**, 104 (2018). https://doi.org/10.12785/ijtfst/070302.
31. J. O. Emegha, C. M. Okafor, and K. E. Ukhurebor, Walailak J. Sci. Tech. (WJST) **18**, 9535 (2021). https://doi.org/10.48048/wjst.2021.9535.
32. A. V. Babalola, V. Oluwasusi, V. A. Owoeye, J. O. Emegha, D. A. Pelemo, A. Y. Fasasi, U. M. Gurku, S. O. Alayande, S. Yusuf, and B. Saje M, Heliyon **10**, e23190 (2024). https://doi.org/10.1016/j.heliyon.2023.e23190.
33. M. K. Khalaf, I. A. Mohammed Ali, M. J. Dathaan, and M. I. Hamil, Egyptian J. Chem. **64**, 5111 (2021). https://doi.org/10.21608/ejchem.2021.66410.3425.
34. M. Julkarnain, J. Hossain, K. Sharif, and K. Khan, J. Optoelect. Adv. Mat. **13**, 485 (2011).
35. A. Hassen, S. El-Sayed, W. Morsi, and A. El Sayed, J. Adv. Phys. **4**, 571 (2014).
36. A. S. Hassanien and I. M. El Radaf, Phys B Cond. Matt.. **585**, 412110 (2020). https://doi.org/10.1016/j.physb.2020.412110.
37. N. Habubi, S. Oboudi, and S. Chiad, J. Nano Elect. Phys. **4**, 04008 (2012).
38. A. F. Qasrawi and A. A. Hamamdah, Microwav. Opt. Tech. Lett. **62**, 1453 (2020). https://doi.org/10.1002/mop.32192.
39. M. K. Khalaf, D. S. A. Al-Kader, and J. M. Salh, IOP Conf. Ser.: Mater. Sci. Eng. **1105**, 012064 (2021). https://doi.org/10.1088/1757-899X/1105/1/012064.

توليف الجسيمات النانوية للنحاس: سلينيوم باستخدام نفاث بلازما الضغط الجوي وخصائصها البصرية

دعاء رفعت جاسم[1] ورامز احمد الانصاري[2] وبان حسن عادل[2]
[1]قسم الأدلة الجنائية كلية العلوم جامعة النهرين، بغداد، العراق
[2]قسم الفيزياء، كلية العلوم للبنات، جامعة بغداد، بغداد، العراق

الخلاصة
أُستُخدمت جسيمات سيلينيد النحاس النانوية (Cu:Se) المُنتجة في تجارب الكشف عن الأشعة فوق البنفسجية وفي مستشعرات الغاز. تم تحضير جسيمات نانوية من Cu:Se بنسب مختلفة (1:9، 2:8، و3:7) باستخدام تقنية نفث البلازما تحت الضغط الجوي. تناولت الدراسة الخصائص البصرية لجسيمات Cu:Se النانوية باستخدام تحليلات حيود الأشعة السينية (XRD)، والتي أظهرت أن إضافة المزيد من Se جعل البلورات أكبر. أُجريت مطيافية الأشعة فوق البنفسجية-المرئية وحساب طاقة فجوة النطاق. أسفرت جميع النسب عن قيم نفاذية عالية، تتراوح من 80% إلى 95%. وُجد أن طاقة فجوة النطاق هي 3.80، و3.25، و4.17 إلكترون فولت لنسب Cu:Se البالغة 1:9، و2:8، و3:7، على التوالي، وهي قيم نموذجية وممتازة لأشباه الموصلات. أظهرت جسيمات Cu:Se النانوية المُنتجة خصائص بصرية جيدة. إن الامتصاص البصري لجسيمات النانو Cu:Se يقع في نطاق واسع من الطول الموجي من 200 إلى 350 نانومتر، وهو مناسب لمواد امتصاص الأشعة فوق البنفسجية.

الكلمات المفتاحية: جسيمات نانوية من النحاس والسلينيوم، نفث البلازما، مطيافية الأشعة فوق البنفسجية والمرئية، الخواص البصرية، طاقة فجوة النطاق.